LANGMUIR

Biological and Environmental Phenomena at the Interface

Interaction of phosphate with lithium cobalt oxide nanoparticles: a combined spectroscopic and calorimetric study

Elizabeth D. Laudadio, Poorandokht Ilani-Kashkouli, Curtis M Green, Nadine Kabengi, and Robert J Hamers

Langmuir, **Just Accepted Manuscript** • DOI: 10.1021/acs.langmuir.9b02708 • Publication Date (Web): 21 Nov 2019

Interaction of phosphate with lithium cobalt oxide nanoparticles: a combined spectroscopic and calorimetric study

Elizabeth D. Laudadio[†], Poorandokht Ilani-Kashkouli[ǁ,‡], Curtis M. Green[†], Nadine J. Kabengi[ǁ,‡], Robert J. Hamers[†*]

[†] Department of Chemistry, University of Wisconsin, Madison, WI 53706
Department of Chemistry, Georgia State University, Atlanta, GA 30303
[‡] Department of Geosciences, Georgia State University, Atlanta, GA 30303

ABSTRACT: Adsorption of small ions such as phosphate to the surfaces of metal oxides can significantly alter the behavior of these materials, especially when present in nanoscale form. Lithium cobalt oxide is a good model system for understanding small-molecule interactions with emerging nanomaterials because of its widespread use in lithium ion batteries and its known activity as a water oxidation catalyst. Here we present a thermodynamic analysis of phosphate adsorption to $LiCoO_2$ and corroborate the results with additional in situ techniques, including zeta potential measurements and ATR-FTIR, at pH values relevant to potential environmental release scenarios. Flow microcalorimetry measurements of phosphate interaction with $LiCoO_2$ at pH 7.4 show that there are two distinct exothermic processes taking place. Time-sequence in situ ATR-FTIR with two-dimensional correlation analysis reveals the spectroscopic signatures of these processes. We interpret the data as an interaction of phosphate with $LiCoO_2$ that occurs through the release of two water molecules, and is therefore best described as a condensation process rather than a simple adsorption, consistent with prior studies demonstrating that phosphate interaction with highly irreversible. Additional measurements over longer times of 5 months show that phosphate adsorption terminates with one surface layer and that continued transformation over longer periods of time arises from H+/Li+ exchange and slow transformation to a cobalt hydroxide, with phosphate adsorbed to the surface only. To the best of our knowledge, this is the first time that flow microcalorimetry and two-dimensional correlation spectroscopy have been applied in tandem to clarify the specific chemical reactions that occur at the interface of solids and adsorbates.

Introduction

The rapid growth in the use of transition metal oxides in emerging technologies such as energy storage brings with it a desire to understand the chemical transformations that these oxides and other nanomaterials undergo in the environment.[1-4] One of the key challenges in understanding the long-term fate of nanomaterials in the environment is that interaction with aqueous systems, adsorption of ions, and acquisition of surface coatings can all alter nanoparticle properties.[5-8] Lithium cobalt oxide ($LiCoO_2$) is a good model system for investigation as it is representative of the broader class of layered oxides being used in energy storage[9-12] and as catalysts for water oxidation and other reactions.[13-15] The transformation of $LiCoO_2$ and related materials in model environmental and biological systems has been shown to have impacts both on nanomaterial properties and model organisms.[16-20] Phosphate ion is a particularly important model adsorbate because of its well-known role in stabilizing surfaces of geochemical importance and the widespread presence of phosphate in surface waters.[21-23]

One of the key challenges in understanding interaction of phosphate and other small ions with nanomaterials is the difficulty in characterizing the important kinetic and thermodynamics factors that control their interaction. We showed previously that phosphate ion irreversibly adsorbs to $LiCoO_2$, altering the surface charge and therefore the dispersibility of the nanomaterials in aqueous solutions.[6] To understand the chemical bonding in more detail, chemically specific probes such as time-course in situ infrared spectroscopy can provide information on structure and bonding, while thermodynamic measurements such as microcalorimetry can determine the energetics of ion adsorption.[24-31] Together, these in situ measurements provide new insights into the nature of bonding at complex oxide surfaces and the thermodynamics of ion adsorption.

Here, we present an investigation combining in situ FTIR with in situ flow microcalorimetry to probe the structure and energetics of phosphate ion interaction with nanosheets of $LiCoO_2$ at different pH values relevant to environmental systems.[32-33] The use of high surface area nanoparticles provides the sensitivity needed to investigate adsorption at sub-monolayer coverages, while layered 2D nanosheets expose almost entirely one crystal plane which thereby minimizes heterogeneity of the exposed surfaces.[34-35] To help overcome spectral broadening and analyze the temporal evolution of the spectra, we use two-dimensional correlation analysis of FTIR data obtained as a function of time.[36-38] Our work directly reveals that phosphate adsorption at circumneutral pH occurs by two distinct steps that we interpret as a transition from a monodentate coordinated phosphate to a bidentate coordinated phosphate. This study highlights need for powerful and complimentary in situ techniques to assess all aspects of these interactions.

Experimental

General. All experiments were conducted using ACS reagent grade chemicals, and all aqueous solutions were prepared in ultrapure water (18.2 MΩ) unless otherwise noted. All sonication was performed in a Cole Parmer Ultrasonic Processor operating with a maximum power of 750 W.

$LiCoO_2$ nanoparticle synthesis and characterization. We synthesized sheet-like nanoparticles of $LiCoO_2$ as described previously.[6, 34] Briefly, we synthesized a $Co(OH)_2$ precursor by dropwise addition of 20 mL of 1 M $Co(NO_3)_2 \cdot 6H_2O$ to 420 mL of 0.1 M solution of LiOH, ensuring a [OH] 5% stoichiometric excess for $Co^{2+} + 2OH^- \rightarrow Co(OH)_2$. The precipitate was isolated by centrifuging into a pellet (4696×g, 3 min) and decanting the supernatant. The product was then washed a total of three more times by redispersing in water and collecting the pellet by centrifugation. After the final rinse, we decanted the supernatant and dried the product in a vacuum oven at 30 °C overnight. Once dried, 0.5 g of the $Co(OH)_2$ precursor was massed for the lithiation step. A 20 g mixture of a 6:4 molar ratio of $LiNO_3$:LiOH was heated at 200 °C in a polytetrafluoroethylene container and assembled in a silicone oil bath under magnetic stirring, forming a molten salt flux. The $Co(OH)_2$ precursor was added to the molten salt and after 30 min, the flux was quenched with water. The product was then collected and washed through four cycles of dispersion/isolation via centrifugation in water, as described above. The product was then dried in a vacuum oven at 30 °C overnight.

Characterization of $LiCoO_2$ nanoparticles. We obtained x-ray diffraction (XRD) patterns of the $LiCoO_2$ nanoparticles using a Bruker D8 Advance powder diffractometer with a Cu Kα source and a Lynxeye detector. Concentrated dispersions of $LiCoO_2$ powders in isopropyl alcohol were prepared through ultrasonication. The mixture was then drop-cast onto a zero diffraction plate (MTI Corp) and allowed to dry, forming a uniform film of material. The powder XRD pattern was acquired using a step size of 0.20° and dwell time of 165 s at each point. To characterize nanoparticle morphology using scanning electron microscopy (SEM), $LiCoO_2$ was dispersed in methanol and spin-coated onto low-resistivity (<0.1 Ω•cm) B-doped Si wafers. Images were acquired using a Leo Supra55 VP SEM, 3 kV electron energy, using a secondary electron detector. The morphology of $LiCoO_2$ nanoparticles was further analyzed with a transmission electron microscope (TEM, FEI Tecnai T12) at 120 kV. TEM grids were prepared by drop-casting suspensions of $LiCoO_2$ nanoparticles in water onto a carbon-supported TEM grid, which was allowed to dry overnight. The lithiation state of the $LiCoO_2$ nanoparticles was assessed by digesting the particles in aqua regia (3:1 v/v ratio of 39% HCl and 68% HNO_3, *caution: highly corrosive!)* and analyzing ion concentrations using inductively coupled plasma – optical emission spectroscopy (ICP-OES), yielding a nanoparticle stoichiometry of $Li_{0.92}CoO_2$.

Flow Microcalorimetry. The flow microcalorimeter used in this study was custom-designed and fabricated in the Kabengi laboratory at Georgia State University. A description of the instrumentation and basic operation has been detailed previously.[26-27, 29] Only a brief description outlining the basic principles of obtaining data and experimental procedures relevant to this study is provided here. To prepare samples for microcalorimetry, we homogeneously packed a 10.0 ± 0.5 mg sample of $LiCoO_2$ nanoparticles into a small region of the flow path and equilibrated with 1 mM LiCl at a flow rate of 0.30 ± 0.02 mL/min. During operation, the liquid temperature was continuously monitored by two thermistors flanking the sample holder and the temperature of each thermistor was recorded every 5.0 s. This voltage across the thermistor was amplified and recorded as a function of time. After thermal equilibrium was reached, the input solution was switched to a solution of 0.9 mM LiCl and 0.1 mM LiH_2PO_4, i.e. keeping the total concentration of Li^+ at 1 mM. The differential thermal signal resulting from the interaction of phosphate species with the $LiCoO_2$ sample was recorded, and the calorimetric peak thus obtained numerically integrated and converted to energy units (Joules) by calibrating the instrument response using heat pulses of known energy. The amount of phosphate adsorbed on the surface was determined by a mass balance calculation using the known total mass injected and a measurement of the mass recovered from effluent samples, which were analyzed for total aqueous concentration of phosphate using High-Performance Liquid Chromatography – Ion conductivity (Metrohm, USA).

We probed the interaction of phosphate with $LiCoO_2$ nanoparticles at three pH values: 5.60 ± 0.05, 7.4 ± 0.5, and 9.0 ± 0.5. In order to avoid possible effects due to competitive adsorption that can occur when using buffer solutions, we did not use buffers and instead controlled solution pH by monitoring the value and adjusting as needed using 2 μL increments of 0.1 M LiOH or 0.1 M HCl as needed. Changes in total concentration and ionic strength resulting from pH adjustments were determined to be less than ≤ 1%. The pH of the influent and effluent solutions was monitored to ensure it remained constant during the course of the experiments.

Quantification of phosphate adsorption with X-ray Photoelectron Spectroscopy (XPS). To quantify the adsorption of phosphate onto $LiCoO_2$, we used XPS measurements of photoelectron emission from the P(2p) and Co(2p) levels. We prepared samples for XPS by suspending 5 mg $LiCoO_2$ nanoparticles in 50 mL of a 1 mM Na_2HPO_4 solution at the three pH values studied (pH 5.6, pH 7.4, pH 9.0, pH of solutions adjusted using either 1 M HCl or 1 M NaOH) After suspending for hour, we isolated the particles through centrifugation (4696×g, 5 min), redispersed in water, and isolated again through centrifugation (14104×g) for 5 minutes. The pellet of particles was then dried under vacuum overnight. We pressed the dried particles into indium foil on a copper foil backing to ensure the sample was of homogenous flatness and thickness and could make good electrical contact with the sample holder. XPS spectra were measured using a Thermo Fisher Scientific K-alpha XPS using at a 45° photoelectron takeoff angle, measuring the Li (1s), Co(2p), O(1s), Na(1s), C(1s) and P(2p) peaks. XPS spectra were fit using CasaXPS software.[38] Co(2p) and P(2p) peak areas were used for quantitative analysis of surface coverage using the following equation:

$$Coverage = \frac{A_{P,2p}}{A_{Co,2p}} \times \frac{SF_{Co,2p}}{SF_{P,2p}} \times \frac{Scans_{Co,2p}}{Scans_{P,2p}} \times \rho_{Co,2p} \times \lambda_{Co,2p} \times \cos\theta$$

Where A = peak area, SF = atomic sensitivity factor ($SF_{Co,2p}$ = 18.23529, $SF_{P,2p}$=1.352941), ρ= density of cobalt in $LiCoO_2$ (30 atoms/nm^3), λ = inelastic mean free path (IMFP) of Co electron emitted from $LiCoO_2$ (1.9 nm, calculated from the NIST database[39] via the TPP-2M equation.[39-40]), θ= Angle of the analyzer to the surface normal (45° for the instrument used here). The coverage equation makes the assumption that the adsorbed layer is thinner than the IMFP of a Co(2p) photoelectron, 1.9 nm. Scans refers to the number of scans that were averaged to achieve the total peak area. Spectra were background subtracted with a Shirley function and peaks were fit using a 30% Gaussian, 70% Lorentzian line shape.

Characterization $LiCoO_2$ of nanosheet zeta potential. Dynamic Light Scattering (DLS) and Laser Doppler Microelectrophoresis measurements were taken with a Malvern Zetasizer Nano ZS. A 250 mg/L stock solution of $LiCoO_2$ was prepared in 1 mL of ultrapure water and sonicated for 1 h in a water-cooled cup ultrasonicator (10 s on, 10 s off for 30 min total sonication time) before analysis. DLS measurements were performed on 1 mg/L $LiCoO_2$ suspensions either in 300 μM NaCl as an approximate ionic strength control, or 100 μM Na_2HPO_4 at the pH values studied (pH 5.6, pH 7.4, pH 9.0). The pH values were achieved by additions of microliter quantities of either 1 M HCl or 1 M NaOH. Three size measurements were taken (approximately 6 minutes) followed by three zeta potential measurements (approximately 5 minutes). The data shown are averages of three experimental replicates for each data point. To avoid possible effects of aggregation the the stock $LiCoO_2$ solution was left sonicating between measurements. SEM images of stock solutions before and after sonication show no change in the nanoparticle morphology (Supporting Information, Figure S1).

Preparation of $LiCoO_2$ layers for Attenuated Total Reflectance – FTIR (ATR-FTIR). Thin layers of $LiCoO_2$ were prepared by spin-coating $LiCoO_2$ suspensions onto a zinc selenide (ZnSe) trapezoidal prism acting as a 10-bounce internal reflection element (IRE). We prepared $LiCoO_2$ suspensions of 1000 mg/L in 2 mL methanol. Solutions were sonicated for 1 h in a cup ultrasonicator with cooling water (10 s on, 10 s off for 30 min total sonication time). To ensure that the ZnSe IREs were clean, we rinsed them with water followed by methanol, dried with N_2, and exposed to UV light from a low-pressure Hg grid lamp (UV Products) in air for at least 10 min before use. We then spin-coated the $LiCoO_2$ suspension onto the clean ZnSe IREs using 25 repeated applications of 75 μL each and spinning for 30 s at 1000 rpm after each application. The layer was then stabilized by heating in a box furnace at 400 °C for 5 min. The ZnSe element was allowed to cool for at least 12 h before using. SEM images of $LiCoO_2$ layers prepared on Si wafers using this method show that the nanoparticles are randomly oriented (Supporting Information, Figure S2).

ATR-FTIR studies of phosphate adsorption to $LiCoO_2$ surfaces. ATR-FTIR spectra were acquired using the previously described $LiCoO_2$-coated ZnSe IREs assembled in a flow cell (Specac) using a Bruker Vertex 70 FTIR spectrometer. Spectra were acquired at 4 cm^{-1} resolution, averaging 500 scans per spectrum. The experiment was performed at a fixed pH of 7.4, using solutions of 100 μM Na_2HPO_4 or pH-adjusted water, where pH was controlled by addition of microliter quantities of 1 M HCl or 1 M NaOH as needed. In each experiment, at reference spectrum was obtained after flowing 1 mL of pH 7.4 water over the $LiCoO_2$-coated ZnSe at 0.5 mL/min. After obtaining the water baseline, a solution of 100 μM pH 7.4 Na_2HPO_4 was then flowed (0.5 mL/min) while continually collecting spectra (approximately 2 minutes per spectrum) for a total duration of 1 hr. All spectra shown here are presented as absorption spectra at different times t, defined as, $A(\tilde{\nu},t) = -log_{10}\left(\frac{I(\tilde{\nu},t)}{I(\tilde{\nu},0)}\right)$ where $I(\tilde{\nu},t)$ is the observed intensity of transmitted light as a function of wavenumber$(\tilde{\nu})$ measured at time t, and t=0 corresponds to the initial spectrum taken after flowing pH 7.4 water over the $LiCoO_2$ film. The volume of the cell is 0.55 mL, and so for each 1 hr interval during which solutions were flowed at 0.5 mL/min, approximately 54 full volume exchanges of the flow cell occurred. FitYK software was used to peak fit the final spectrum.[41]

Two-dimensional correlation spectroscopic analysis of ATR-FTIR data. Two-dimensional correlation spectroscopy (2D-COS) analysis of infrared spectra is a method used to investigate spectral changes as a function of an external perturbation or variable.[36-38] We employed this technique to assess spectral changes as a function of time. Time-course ATR-FTIR spectra were obtained as detailed above. Using a custom program in Igor Pro software, calculated the time-dependent absorption spectra and removed residual baselines in the region of primary interest (1200 - 800 cm^{-1}) by a simple linear fit to the absorbance at the edges of this region (1400 – 750 cm^{-1}). The 2D-COS plots were obtained Fourier-transforming the spectra obtained at different times and taking the cross-correlation in the frequency domain using the equation:

$$\phi_{(\nu_1,\nu_2)} + i\psi_{(\nu_1,\nu_2)} = \frac{1}{\pi T}\sum_{n=0}^{n=N-1} \tilde{Y}_1(\tilde{\nu}_1, \omega = n\omega_0)\tilde{Y}_2^*(\tilde{\nu}_2, \omega = n\omega_0)$$

In this equation, $\tilde{Y}_1(\tilde{\nu}_1,\omega)$ is the Fourier transform (in time) of the absorbance spectra $A(\tilde{\nu},t)$, which were measured at N equally spaced time intervals Δt over a total time T such that $T=n\Delta t$ where $n = 0, \ldots N-1$. We calculated the discrete Fourier transform $\tilde{Y}_1(\tilde{\nu},\omega)$ as:

$$\tilde{Y}_1(\tilde{\nu},\omega) = \frac{1}{2\pi}\sum_{m=0}^{m=N-1} e^{2\pi i m/N} A(\tilde{\nu}, t = n\Delta t)$$

where $\omega = m\omega_0$ (m=0,...,N/2) and $\omega_0 = 2\pi/T$. Note that the frequency ω is related to the times *t* at which the spectra were acquired, while $\tilde{\nu}$ refers to the spectral frequencies as conventionally represented in wavenumbers, cm^{-1}. The resulting complex function yields two-dimensional data, where $\phi_{(\nu_1,\nu_2)}$ is the synchronous 2D correlation plot and $\psi_{(\nu_1,\nu_2)}$ is the asynchronous 2D correlation plot. The synchronous and asynchronous correlation plots can be analyzed via Noda's rules[36], which describe the relationship between the signs of the cross peaks and the changes in spectral intensity.[36-38] Cross-peaks of identical sign in the synchronous plot indicate that the changes in the absorbance of these regions as a function of time either increase or decrease in the same direction, whereas cross-peaks of opposite signs indicate that the changes occur such that one band increases while the other decreases. The sequential order of the changes in bands can then be determined by relating the signs of the synchronous plot to asynchronous plot. If the signs of the features in the asynchronous and synchronous plots are the same, the change in the X axis band ($\tilde{\nu}_1$) occurs before the Y axis band ($\tilde{\nu}_2$). If the signs are opposite, the change in the X axis band ($\tilde{\nu}_1$) occurs after the Y axis band ($\tilde{\nu}_2$). The symmetry properties of the above calculations force the synchronous plot to be symmetric about the diagonal, while the asynchronous plot must be anti-symmetric about the diagonal.

Results and Discussion

$LiCoO_2$ nanoparticle synthesis characterization. Figure 1a shows a representative SEM micrograph of nanoparticles used for this study. SEM reveals a sheet-like morphology of $LiCoO_2$ nanoparticles. Further morphology analysis with TEM

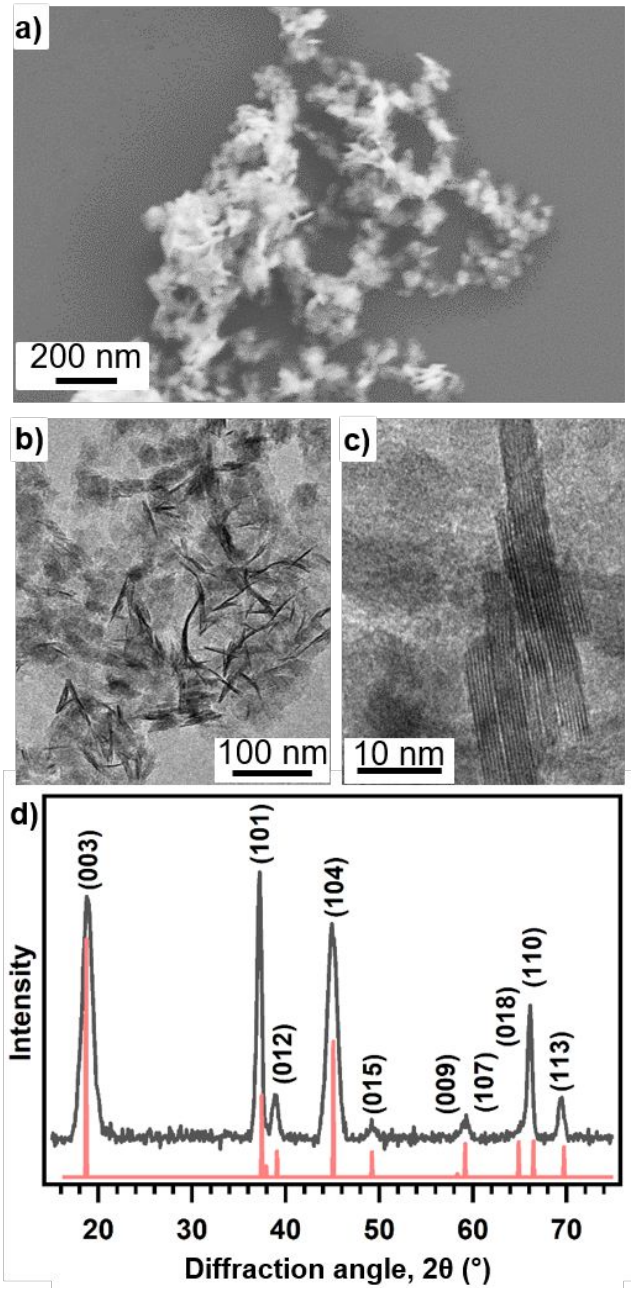

Figure 1. a) scanning electron micrograph of the nanosheets of $LiCoO_2$. b) transmission electron micrograph of $LiCoO_2$. c) higher magnification transmission electron micrograph of $LiCoO_2$ edge-on. d) powder x-ray diffraction pattern of $LiCoO_2$ nanosheets (gray) which can be indexed to the R$\bar{3}$m spacegroup. The pattern from crystallographic information file of single crystal $Li_{0.68}CoO_2$ (pink) is shown for comparison.[32]

is shown in Figure 1b and 1c, where individual particles imaged edge-on reveal the lattice planes of the layered material. Figure 1d shows a powder XRD pattern collected from these particles. The pattern can be indexed to the R$\bar{3}$m space group by comparison of the collected XRD pattern to that of single crystal $LiCoO_2$.[35] While the lack of full separation of the (018) and (110) peaks may indicate the presence of residual spinel phases[42], the inability to resolve these individual peaks could also be due to the peak-broadening that occurs when acquiring XRD patterns of nanoparticles. We expect these particles to be reasonable models for the degradation of the cathode materials in lithium ion batteries, where mechanical fracture following electrochemical cycling is common.[43] We note that while in the pristine material the basal plane of $LiCoO_2$ is terminated in lithium, because the material is an intercalation compound, the lithium ions are highly mobile and likely to undergo Li^+/H^+ exchange in solution. This has been demonstrated experimentally[44] as well as computationally.[45] Analysis of lithium release from $LiCoO_2$ in the presence of phosphate shows that approximately 30% of the total lithium is released, which we believe is consistent with the total amount of lithium released being mostly limited to the surface lithium (Supporting Information, Figure S3). We therefore expect the surface of the materials in aqueous solutions to be hydroxylated instead of lithium terminated.

Energetics of interaction from flow microcalorimetry.

Figure 2a shows microcalorimetry data obtained from phosphate exposure to $LiCoO_2$ at three different values of pH; pH 5.6 (pink trace), pH 7.4 (green trace), and pH 9.0 (blue trace). In each case, when LiCl is substituted with Li_2HPO_4-containing solutions, a positive calorimetric signal is detected. This sign is consistent with heat being released following phosphate interaction with $LiCoO_2$, indicating a negative enthalpy of adsorption. However, the shapes of the heat release profiles at each pH are significantly different.

This is most obvious at pH 7.4, where the heat release is greatest in magnitude at each time point and shows two distinct features: an initial heat of release over ~20 minutes, followed by a slower release of heat over ~40-60 minutes. The calorimetric signal can be converted to a heat of adsorption (Q_{ads}) by integrating the curves and using the calibration of an internal standard to convert V•min to mJ, which was then normalized by the mass of the $LiCoO_2$ in each experiment.

Figure 2b shows the values of Q_{ads} obtained at each pH studied. The value of Q_{ads} at pH 7.4 is -5.16 mJ/mg, which is approximately twice of what is released at pH 5.6, -2.28 mJ/mg. Q_{ads} at pH 9.0 is the smallest in magnitude, at -0.90 mJ/mg.

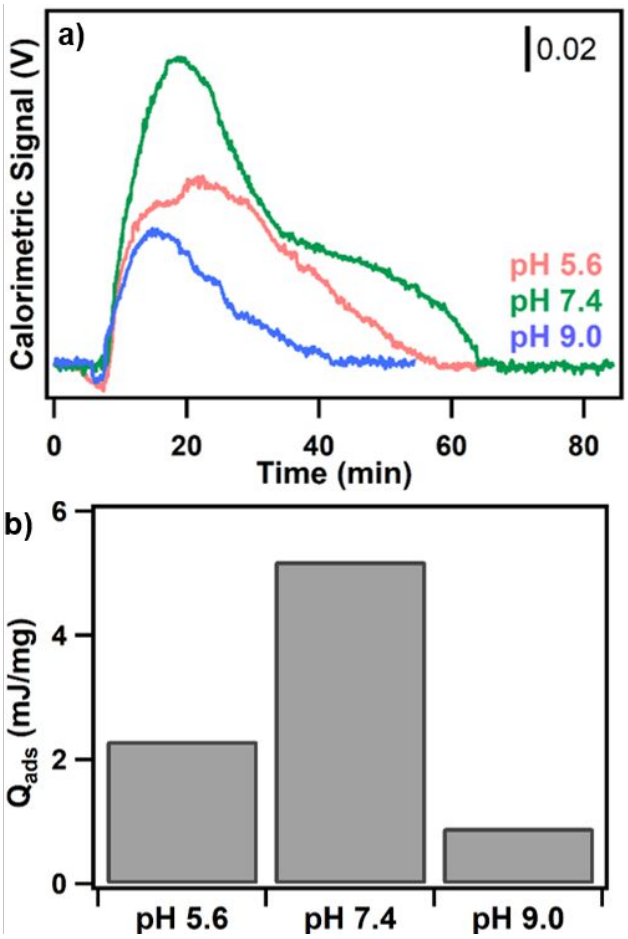

Figure 2. a) Calorimetric signals for phosphate interaction with $LiCoO_2$ at pH 5.6 (pink trace), 7.4 (green trace), and 9.0 (blue trace) as a function of time. An increase in voltage resulting in a positive peak corresponds to a release of energy and hence an exothermic reaction. b) heats of adsorption (Q_{ads}) obtained by converting the calorimetric peak area to energy units and normalizing by sample mass.

Determination of Surface Coverage. We determined the amount of phosphate adsorbed to $LiCoO_2$ using two complementary approaches. In one, we collected the effluent from the microcalorimetry apparatus and measured phosphate concentration (via ion chromatography) and effluent volume to get the total number of moles of phosphate in the effluent, and subtracted this from the total moles of phosphate introduced into the system during the same time interval. The resulting difference represents the amount of phosphate adsorbed to the $LiCoO_2$ nanoparticles during the microcalorimetry experiment. Figure 3a shows that the amount adsorbed at pH 5.6 and 7.4 were similar to one another, while the amount adsorbed at pH 9.0 was much lower.

We also quantified the phosphate adsorption using XPS by exposing samples to phosphate at different pH values. We determined the absolute surface coverage of phosphorus using the area of the Co(2p) peaks as an internal standard (Supporting Information, Figure S4) which were analyzed to yield the coverage values shown in Figure 3. We confirmed the coverage using the bulk O(1s) intensity as an internal standard, with nearly identical results. These data show that the phosphate coverage (in atoms phosphorus / nm^2) decreases from 1.4 at pH 5.6 to 0.6 at pH 9.0. A single-factor ANOVA test reveals that the phosphate coverage at pH 5.6 and pH 7.4 are indistinguishable, while the lower coverage at pH 9.0 is

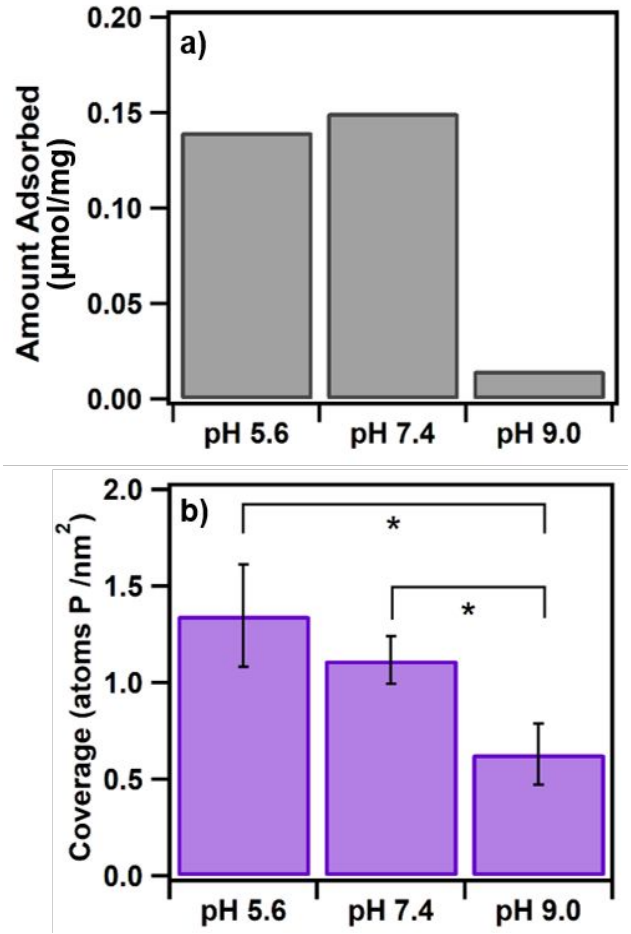

Figure 3. Phosphate coverage on $LiCoO_2$ as a function of pH. a) phosphate coverage in units of µmol/mg $LiCoO_2$, as determined from ion chromatography following calorimetry. b) phosphate coverage in atoms P/nm^2 as determined from XPS. Asterisks indicate significant difference between means as based on a single-factor ANOVA test.

statistically lower than the values at pH 5.6 and pH 7.5 ($p < 0.02$).

Both the microcalorimetry data and XPS data show that the phosphate coverage is similar at pH 5.6 and 7.4, but significantly lower at pH 9. By using the specific surface area of the nanoparticles as determined from Brunauer-Emmett-Teller adsorption analysis, the microcalorimetry data can be represented as an atomic number density (atoms / nm^2), the same units of the coverages from XPS analysis (detailed calculation in Supporting Information). Coverage values from ion chromatography when converted to units of atoms/nm^2 are 0.6 at pH 5.6, 0.7 at pH 7.4, and 0.07 at pH 9.0. These values are slightly lower than those determined by XPS, potentially reflecting the fact that in the microcalorimetry experiments some of the surface area that is accessible to gaseous species (as in BET analysis) maybe inaccessible in the geometry of the microcalorimetry experiment. Nevertheless, one important outcome of these experiments is that since the amount of phosphate adsorbed at pH 7.4 is comparable to that adsorbed at pH 5.6, we conclude that the higher amount of heat evolved at pH 7.4 cannot be accounted for on the basis of greater

phosphate adsorption, but rather indicates that the specific chemical processes occurring at pH 7.4 are more exothermic.

Analysis of apparent zeta potential as an indication of relative surface charge. We characterized the influence of phosphate exposure on the nanoparticle surface charge using measurements of the electrophoretic mobility and apparent zeta potential. Because our nanoparticles have a flake-like geometry, the hydrodynamic equations typically used to relate mobility to zeta potential are not strictly applicable.[46-47] We therefore include the measured electrophoretic mobilities values and also the apparent zeta potential as derived from Henry's Equation, which is defined as $\frac{U}{E} = \frac{2\varepsilon\zeta F(\kappa\alpha)}{3\eta}$, where U/E is the electrophoretic mobility, ζ is the apparent zeta potential, ε is the solvent dielectric permittivity constant, η is the viscosity of the solvent, and F(κα) is Henry's function, which is approximated to 3/2 in the Smoluchowski model, which is most commonly used for nanomaterials in polar solvent.[46-47]

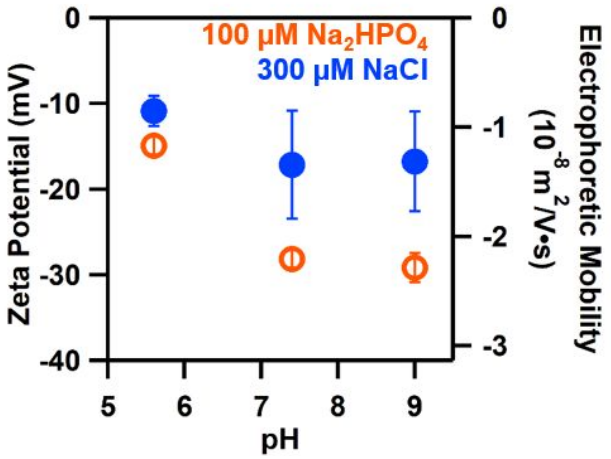

Figure 4. apparent zeta potential (left axis) and electrophoretic mobilities (right axis) of $LiCoO_2$ in 100 μM Na_2HPO_4 (orange, open markers) and comparable ionic strength non-interacting salt, 300 μM NaCl (blue, closed markers) as a function of pH.

To control for the influence of solution-phase ions on apparent zeta potential measurements, we also did control experiments using a NaCl solution having a similar ionic strength to the phosphate solutions used here. Figure 4 shows the mobilities and apparent zeta potential of $LiCoO_2$ nanoparticles in 100 μM Na_2HPO_4 (open, orange circles) and in a control experiment consisting of 300 μM NaCl (filled blue circles) at pH 5.6, 7.4 and 9.0. At all pHs studied here, the $LiCoO_2$ nanoparticles have a net negative charge in phosphate and in the NaCl control solution. At pH 5.6, the zeta potential is nearly the same in both NaCl and phosphate, while at higher pH values the $LiCoO_2$ nanoparticles have higher mobility (more negative apparent zeta potential) than those in the NaCl control. We note that the apparent zeta potential of the $LiCoO_2$ nanoparticles in the phosphate solution are approximately -30 mV at the two higher pH values, a value often considered a threshold for forming stable colloids.[48-49] Dynamic light scattering measurements show that neither pH nor presence of phosphate impact the diffusion coefficient of $LiCoO_2$ under these conditions (Supporting Information, Figure S5). When this result is considered in conjunction with the data showing that adsorption of phosphate onto $LiCoO_2$ at pH 7.4 is higher than at pH 9.0, the combination of these results, and the exotherm from the calorimetry experiment, suggest that the difference in the interaction of phosphate with $LiCoO_2$ at pH 7.4 cannot be explained by the surface charge of $LiCoO_2$ as a function of pH. There is a higher amount of phosphate adsorbed, and higher heat released from phosphate interaction with $LiCoO_2$ at pH 7.4 compared with pH 9.0, despite the surface charge of $LiCoO_2$ both in the presence and absence of phosphate being indistinguishable between pHs 7.4 and 9.0.

ATR-FTIR and 2D-COS analysis of the evolution of phosphate vibrational modes on $LiCoO_2$. In order to understand the thermodynamic trajectory of phosphate interaction with $LiCoO_2$ at pH 7.4, we used ATR-FTIR to characterize the geometry of phosphate adsorbed to $LiCoO_2$ over time. Figure 5a shows the final spectrum after the one hour of exposure of phosphate to $LiCoO_2$. Consistent with our prior study[6], adsorption of phosphate species to $LiCoO_2$ results in a single broad feature in the region from 1200 – 800 cm^{-1} that is composed of multiple vibrational contributions. Here we show that the broad feature can be fit to five individual peaks at 1143, 1085, 1032, 993 and 956 cm^{-1}. By comparing the number and frequency of the vibrational modes on the surface of $LiCoO_2$ to a free $H_2PO_4^-$ molecule, the final geometry of phosphate on the surface of $LiCoO_2$ can be assigned to a bidentate structure.[50-51] A bidentate geometry on the surface of $LiCoO_2$ has the same symmetry as that of the $H_2PO_4^-$ molecule (i.e., $Co_2PO_4^-$), and therefore should have the same number of primary infrared active vibrational modes.

The two peaks between 1000 – 900 cm^{-1} are analogous to HO-P asymmetric and symmetric vibrations in $H_2PO_4^-$, shifted to higher wavenumbers on the surface of $LiCoO_2$ due to the difference in bond strength of CoO-P versus HO-P.[50-51] Likewise, the two peaks between 1100 – 1000 cm^{-1} are analogous to the symmetric and asymmetric $(HO)_2PO_2$ vibrations in $H_2PO_4^-$, shifted to lower wavenumbers when bound to $LiCoO_2$ due to the weaker bond strength of $(CoO)_2PO_2$ versus $(HO)_2PO_2$.[50-51] The fifth peak between 1200 – 1100 cm^{-1} can be assigned to a P-OH bending vibration which has been reported to be both broad and weak in spectra.[52] This final binding geometry assignment is consistent with our previous work, though those experiments were done at lower phosphate concentrations.[6]

A close examination of the spectra collected as a function of time (Supporting Information, Figure S6) shows that the structure of the phosphate peak changes with time, indicating that there are time-dependent changes in the phosphate geometry on the $LiCoO_2$ surface that occur over the timescale of one hour. These changes are challenging to interpret by eye, as they are subtle differences in the overall broad feature. Employing 2D-COS analysis allows for these subtle differences to be clarified over time. The spectra as obtained over the course of phosphate exposure consist of vibrational contributions from both the adsorbed phosphate and the free phosphate in solution within the penetration depth of the ATR element Because 2D-COS is only sensitive to changes in vibrational modes over time, the confounding signal from the free phosphate is effectively removed in the analysis.

The synchronous plot of the 2D-COS analysis is shown in Figure 5b, and the asynchronous plot is shown in Figure 5c. The symmetry properties of the correlation analysis dictate that the synchronous spectrum must be symmetric with respect to reflection about the diagonal, while the asynchronous spectrum is antisymmetric (i.e., inverts the sign) across the diagonal. As a result, the information in the upper-left half-

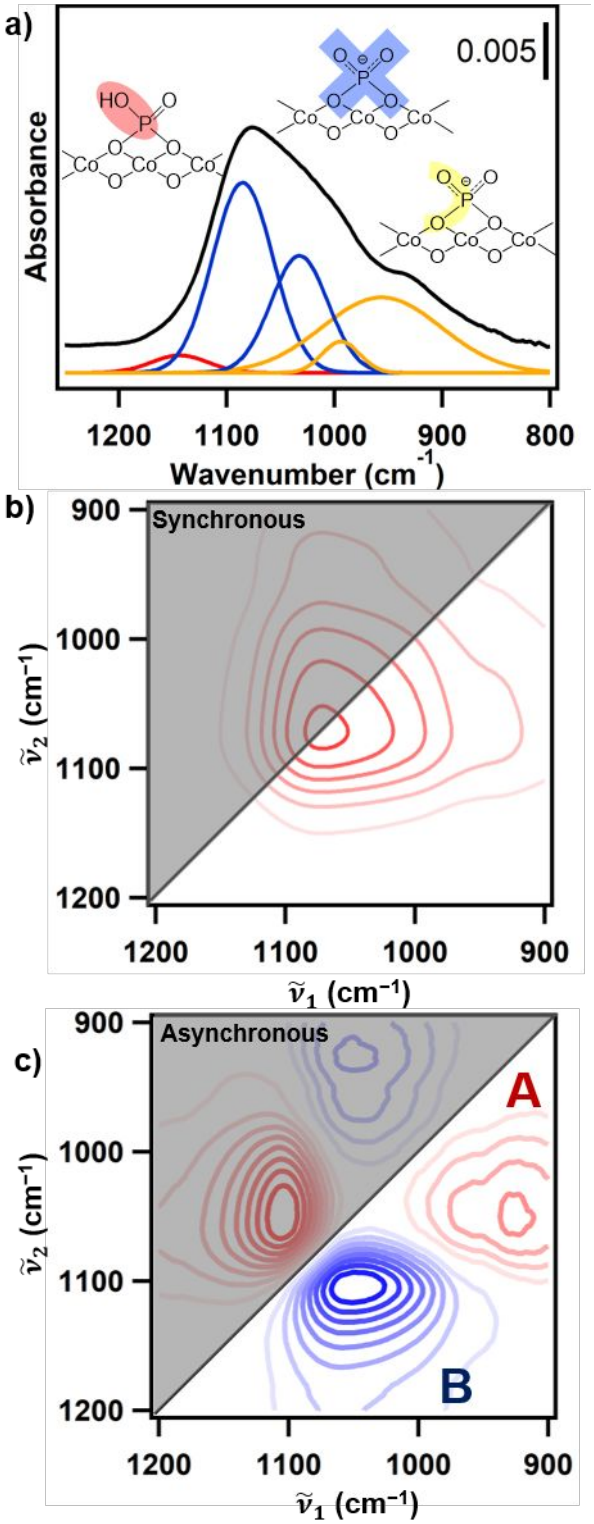

Figure 5. a) ATR-FTIR spectrum of phosphate on $LiCoO_2$, indicating the vibrational modes in each region. b) synchronous 2D correlation plot for phosphate exposure to $LiCoO_2$. c) asynchronous 2D correlation plot for phosphate exposure to $LiCoO_2$. Positive contours are red, negative contours are blue, with darker shades indicating larger values.

space and lower-right half-space of the plot is redundant. We therefore confine our discussion to the lower-right half-space of each plot.

The synchronous plot in Figure 5b shows a single large positive (red) feature in the region from 1200 – 900 cm^{-1}. The single positive feature indicates that the absorbance of this entire region increasing monotonically as a function of time. This is consistent with the evolution of the one-dimensional spectra over time as shown in Figure S4, where the absorbance of the entire region is seen to be increasing between each spectrum collected over the time interval.

Analysis of the location and sign of the features in the asynchronous plot in Figure 5c yields information about the sequential order in which the absorption peaks occur. The asynchronous plot shows two major features. The existence of these correlated features is evidence that the vibrational modes of phosphate, and thus the geometry of phosphate on the surface of $LiCoO_2$, is evolving with time. This is consistent with the microcalorimetry data that indicates the interaction of phosphate and $LiCoO_2$ occurs in two separate exothermic steps over time.

There is a positive (red) peak in the asynchronous plot that is centered at $\tilde{\nu}_1$ = 940 – 910 cm^{-1} and $\tilde{\nu}_2$ = 1065 – 1030 cm^{-1}, labeled A in Figure 5c. The positive sign of this feature indicates that the absorbance of the modes at 940 – 910 cm^{-1} is increasing before those at 1065 – 1030 cm^{-1}. The vibrational analysis conducted on the one-dimensional spectrum in Figure 5a revealed two peaks between 1000 – 900 cm^{-1} that correspond to CoO-P vibrations, and two peaks between 1100 – 1000 cm^{-1} that correspond to $(CoO)_2PO_2$ vibrations, as have been assigned in related studies on different materials.[50-51] The appearance of CoO-P vibrations before $(CoO)_2PO_2$ vibrations may indicate that modes related to phosphate binding to $LiCoO_2$ through a single cobalt on the surface are occurring before the modes related to phosphate bound to $LiCoO_2$ through two cobalt atoms, as is such in the final bidentate structure.

The remaining feature in the asynchronous plot is a negative (blue) peak centered at $\tilde{\nu}_1$ = 1080 – 1000 cm^{-1} and $\tilde{\nu}_2$ = 1130 – 1080 cm^{-1}, labeled B in Figure 5c. The negative value of this peak indicates that the vibrational modes at 1130 – 1080 cm^{-1} increase in intensity before the modes at 1080 – 1000 cm^{-1}. The vibrational analysis of the one-dimensional spectrum in Figure 5a revealed two peaks between 1100 – 1000 cm^{-1} that correspond to $(CoO)_2PO_2$ vibrations, and a single peak between 1200 – 1100 cm^{-1} that corresponds to P-OH bending vibrations, as have been assigned in related studies on different materials.[50-51]

Our interpretation of this negative feature (labeled B in the asynchronous plot) is that the vibrational modes relating to the P-OH bending motion are occurring in the spectra before the vibrational modes relating to the $(CoO)_2PO_2$ vibrations of the final bidentate surface structure. The two features in the asynchronous plot are consistent with CoO-P and P-OH vibrations both growing into the spectra before $(CoO)_2PO_2$ vibrations. This information, in combination with the flow microcalorimetry results, allow us to propose a hypothesized mechanism of phosphate adsorption onto $LiCoO_2$ at pH 7.4.

Proposed mechanism. Taking into consideration all of the data presented here, we propose a mechanism for how phosphate interacts with the $LiCoO_2$ surface at pH 7.4. Both XPS and flow calorimetry calculations of phosphate surface coverage on $LiCoO_2$ revealed that a comparable amount of phosphorus is retained on the surface of $LiCoO_2$ at both pH 5.6 and pH 7.4, indicating that the noticeable difference in the profile of the heat release in the flow microcalorimetry data cannot be due to a larger amount of phosphate adsorbing to the surface. The 2D-COS analysis revealed correlations in time

Scheme 1. Proposed mechanism of phosphate interaction with $LiCoO_2$ at pH 7.4. A) $H_2PO_4^-$ forms a hydrogen bond to a protonated oxygen on the surface of $LiCoO_2$. A subsequent phosphoryl transfer reaction releases a water molecule and a covalent bond between phosphate and the surface is formed. B) a second hydrogen bond between the surface $CoHPO_4^-$ and another protonated group on the surface forms, and a second phosphoryl transfer reaction releases a second water molecule. C) the final structure, a bidentate, deprotonated phosphate coordinated to the surface of $LiCoO_2$.

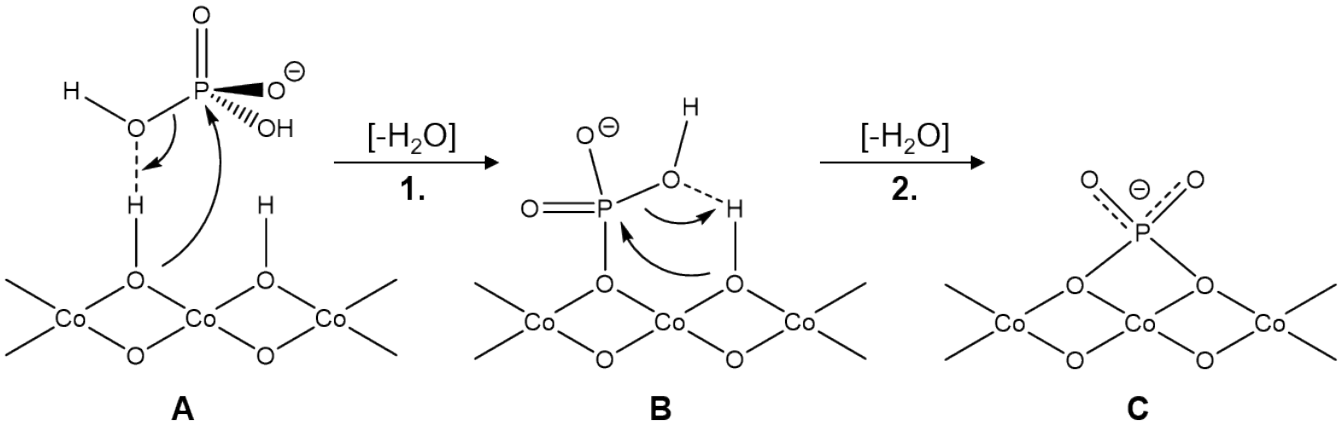

evolution between the vibrational modes of phosphate, indicating that both P-OH bending modes and CoO-P modes occur before the $(CoO)_2PO_2$ vibrations. Scheme 1 shows the proposed mechanism of interaction based on the whole of the data presented here. We propose that phosphate in the form of $H_2PO_4^-$ (roughly 50% of phosphate present at pH 7.4) first forms a hydrogen bond with the hydroxylated $LiCoO_2$ surface as shown in the step labeled A of Scheme 1. Density functional theory calculations have shown that this step is thermodynamically favorable on a partially hydroxylated $LiCoO_2$ surface.[45] Following hydrogen bond formation, a phosphoryl transfer reaction results in the loss of water and formation of a covalent bond between the phosphate and the $LiCoO_2$ surface, forming a monodentate structure on the surface as shown in the second structure of Scheme 1 labeled B. The loss of water is an exothermic process, and we attribute the first peak in the flow calorimetry data to this surface reaction. At this point, the adsorbed phosphate molecule can exhibit both CoO-P stretching modes and P-OH bending modes, consistent with these modes developing first in the 2D-COS plots of the FTIR spectra. The phosphate in the structure labeled "B" can then further react with another hydroxylated group on $LiCoO_2$ through a subsequent phosphoryl transfer reaction. Another molecule of water is released, consistent with the second exothermic process identified in the flow microcalorimetry. The phosphate molecule is then in a bidentate geometry on the $LiCoO_2$ surface, consistent with the 2D-COS analysis showing that the $(CoO)_2PO_2$ vibrations grow into the spectra later than the other modes. If the two distinct features in the calorimetry trace are fit separately, the area under each curve is comparable, consistent with the exothermic process at each step resulting from a similar reaction: the release of a water molecule. The P-OH bending vibrations do not decrease in the spectra, which may suggest that the phosphate can be further protonated once adsorbed or that not all the monodentate structures are converted to bidentate. The observation that this bimodal interaction is not observed at other pH values may suggest that factors such as concentration of the different dissolved forms of hydrogen phosphate, relative proportions of hydroxylated groups on $LiCoO_2$, as well as exposure time and flow rate are all likely to play a role in how the interaction of phosphate with $LiCoO_2$ surfaces progress with time. At pH 5.6, we speculate that the Step 1 of our proposed mechanism may occur more quickly due to the higher percentage of $H_2PO_4^-$ (~98%) and more positive surface charge of $LiCoO_2$, such that the available surface sites are filled before Step 2 can occur. At pH 9.0, only ~2% of the phosphate exists as $H_2PO_4^-$. We suspect that the more significant electrostatic repulsion between the surface and the dominant HPO_4^{2-} versus $H_2PO_4^-$ may be a factor in the lower coverage observed.

The oxygen-oxygen distance between nearest-neighbor oxygen atoms in the basal plane of $LiCoO_2$ (2.816 Å) is very similar to the oxygen distances in the orthophosphate molecule, and previous crystallographic comparisons on other materials have shown that the bidentate conformation of phosphate on the surface of other metal oxides is geometrically feasible.[53] The oxygen-oxygen distances in $LiCoO_2$ are further comparable to the oxygen-oxygen bond distances in several bulk cobalt phosphates such as where oxygen-oxygen distances are 2.5 – 2.8 Å on average for cobalt tetrametaphosphate[54], cobalt phosphate[55], and cobalt diphosphate,[56] which further supports the model of a bidentate surface adsorption and formation of an inorganic cobalt phosphate coating presented here.[54-56]

While the concentrations of phosphate studied here are higher than typical environmental concentrations, the final coordination of phosphate on the surface of $LiCoO_2$ at 100 μM phosphate is the same as we determined in our previous study at a more environmentally relevant concentration of 1 μM phosphate. The model present here is consistent with our previous study in which we found that phosphate adsorption occurs even at environmentally relevant concentration of $<10^{-4}$ M and that this adsorption was irreversible, demonstrated by the fact that rinsing phosphate-exposed $LiCoO_2$ with water did not dislodge phosphate once adsorbed to the surface. Our present result indicate that the reason for this irreversible behavior is that phosphate interaction is not a simple adsorption process but is better described as a condensation reaction in which the free energy change associated with formation and release of water molecules drives the interaction to a new structure like that in Scheme 1.

The irreversible, exothermic nature of phosphate surface adsorption suggests that possibility that adsorption of phosphate to $LiCoO_2$ could be the first step of a transformation to a new bulk cobalt phosphate composition. To test whether the initial adsorption investigated here continues to form a bulk phosphate over longer periods of time, we conducted a limited number of experiments using nanoparticles that were exposed to 1 mM Na_2HPO_4 at pH 7.4 for 5 months. XPS analysis of nanoparticles after 5 months of exposure (Supporting Information, Figure S7a) yields coverage values on the order of ~1 atom P/nm^2, comparable to the values obtained after just one hour of exposure. This similarity suggests that phosphate adsorption is limited to the exterior surface of the nanomaterials.

SEM micrographs (Supporting Information, Figure S7b) show that the flake-like morphology is retained after long-term phosphate exposure, evidence of a self-limiting phosphate adsorption that does not alter the overall morphology of the material. However, powder XRD data (Supporting Information, Figure S7c) show that long-term exposure leads to a significant broadening of the diffraction features. Prior studies have shown that $LiCoO_2$ can easily undergo Li^+/H^+ site exchange by releasing Li^+ and intercalating H^+ to conserve overall charge neutrality, and that this occurs without disruption of the particle morphology.[57-58] Our data suggest that the diffraction peak broadening and associated loss of crystallinity arises from this H^+/Li^+ site exchange, forming a transformed material whose bulk composition more closely resembles that of a cobalt hydroxide, while the surface composition resembles a cobalt phosphate, with phosphate ions remaining adsorbed at the surface only.

Conclusions

The studies presented here demonstrate that the combination of flow microcalorimetry and FTIR can provide unique molecular-level insights into the nature of molecular adsorption and reaction processes at solid-liquid interfaces. In the case of $LiCoO_2$, flow microcalorimetry data reveal two distinct exothermic surface processes occurring at pH 7.4. By combining flow microcalorimetry with in situ FTIR and correlation analysis, our data indicate that phosphate and $LiCoO_2$ interact via a two-step process at pH 7.4, in which evolution of water at two distinct steps in the adsorption process gives rise to two exothermic peaks in the flow calorimetry data. While this study demonstrates the power of both flow microcalorimetry and time-sequential FTIR measurements with 2D-COS analysis, it highlights the depth of information that is obtained by using the two techniques in conjunction with one another that is not possible with either one independently.

Our data indicate that the interaction of phosphate with $LiCoO_2$ is best described as a condensation reaction in which the release of water molecules provides a strong driving force for reaction, but this reaction is limited to only a surface layer and does not continue toward a bulk transformation under ambient conditions. Understanding the interaction of anions such as phosphate with transition metal oxide nanomaterials may have important consequences for understanding the long-term environmental impact associated with accidental release or improper disposal of nanomaterials. Since there is currently no large-scale infrastructure for recycling of $LiCoO_2$ and related transition metal oxides used in lithium ion batteries, understanding the transformations of these materials can help to predict the potential environmental impact associated with their overall life cycle.

ASSOCIATED CONTENT

Supporting Information. Additional methods, analysis and figures as described in the main text are available in the supporting information. This material is available free of charge via the Internet at http://pubs.acs.org.

AUTHOR INFORMATION

Corresponding Author

*Email: rjhamers@wisc.edu

ORCID

Elizabeth D. Laudadio: 0000-0002-3522-1722
Poorandokht Ilani-Kashkouli: 0000-0002-9711-2089
Curtis M. Green: 0000-0001-7236-7408
Nadine Kabengi: 0000-0002-1901-0992
Robert J. Hamers: 0000-0003-3821-9625

Notes

These authors declare no competing interest.

ACKNOWLEDGMENT

This work was supported by National Science Foundation Center for Chemical Innovation Program grant CHE-1503408 for the Center for Sustainable Nanotechnology. E.D.L. is supported by the National Science Foundation Graduate Research Fellowship Program under Grant No. DGE-1747503. Additional support to E.D.L. was also provided by the Graduate School and the Office of the Vice Chancellor for Research and Graduate Education at the University of Wisconsin-Madison with funding from the Wisconsin Alumni Research Foundation. The authors gratefully acknowledge use of facilities and instrumentation supported by NSF through the University of Wisconsin Materials Research Science and Engineering Center (DMR-1720415).

REFERENCES

1. Murphy, C. J.; Vartanian, A. M.; Geiger, F. M.; Hamers, R. J.; Pedersen, J.; Cui, Q.; Haynes, C. L.; Carlson, E. E.; Hernandez, R.; Klaper, R. D.; Orr, G.; Rosenzweig, Z. e., Biological responses to engineered nanomaterials: Needs for the next decade. *ACS Cent. Sci.* **2015,** *1*, 117-123.
2. Grassian, V. H.; Haes, A. J.; Mudunkotuwa, I. A.; Demokritou, P.; Kane, A. B.; Murphy, C. J.; Hutchison, J. E.; Isaacs, J. A.; Jun, Y.-S.; Karn, B.; Khondaker, S. I.; Larsen, S. C.; Lau, B. L. T.; Pettibone, J. M.; Sadik, O. A.; Saleh, N. B.; Teague, C., Nanoehs – defining fundamental science needs: No easy feat when the simple itself is complex. *Environ. Sci.: Nano* **2016,** *3*, 15-27.
3. Keller, A. A.; McFerran, S.; Lazareva, A.; Suh, S., Global life cycle releases of engineered nanomaterials. *J Nanopart Res* **2013,** *15*, 1692-1709.
4. Lowry, G. V.; Gregory, K. B.; Apte, S. C.; Lead, J. R., Transformations of nanomaterials in the environment. *Environ. Sci. Technol.* **2012,** *46*, 6893-6899.
5. Mensch, A. C.; Hernandez, R. T.; Kuether, J. E.; Torelli, M. D.; Feng, Z. V.; Hamers, R. J.; Pedersen, J. A., Natural organic matter concentration impacts the interaction of functionalized diamond nanoparticles with model and actual bacterial membranes. *Environ. Sci. Technol.* **2017,** *51*, 11075-11084.
6. Laudadio, E. D.; Bennett, J. W.; Green, C. M.; Mason, S. E.; Hamers, R. J., Impact of phosphate adsorption on complex cobalt

oxide nanoparticle dispersibility in aqueous media. *Environ. Sci. Technol.* **2018,** *52*, 10186-10195.
7. Ho, T. A.; Greathouse, J. A.; Lee, A. S.; Criscenti, L. J., Enhanced ion adsorption on mineral nanoparticles. *Langmuir* **2018,** *34*, 5926-5934.
8. Ho, T. A.; Criscenti, L. J.; Greathouse, J. A., Revealing transition states during the hydration of clay minerals. *J. Phys. Chem. Lett.* **2019,** *10*, 3704-3709.
9. Ellingsen, L. A.; Hung, C. R.; Majeau-Bettez, G.; Singh, B.; Chen, Z.; Whittingham, M. S.; Stromman, A. H., Nanotechnology for environmentally sustainable electromobility. *Nat Nanotechnol* **2016,** *11*, 1039-1051.
10. Whittingham, M. S., Lithium batteries and cathode materials. *Chem. Rev.* **2004,** *104*, 4271-4301.
11. Notter, D. A.; Gauch, M.; R., W.; Wagner, P.; Stamp, A.; Zah, R.; Althaus, H.-J., Contribution of li-ion batteries to the environmental impact of electric vehicles. *Environ. Sci. Technol.* **2010,** *44*, 6550-6556.
12. Dunn, J. B.; Gaines, L.; Kelly, J. C.; James, C.; Gallagher, K. G., The significance of Li-ion batteries in electric vehicle life-cycle energy and emissions and recycling's role in its reduction. *Energy Environ. Sci.* **2015,** *8*, 158-168.
13. Kanan, M. W.; Surendranath, Y.; Nocera, D. G., Cobalt–phosphate oxygen-evolving compound. *Chemical Society Reviews* **2009,** *38*, 109-114.
14. Xiao, X.; Liu, X.; Wang, L.; Zhao, H.; Hu, Z.; He, X.; Li, Y., Licoo2 nanoplates with exposed (001) planes and high rate capability for lithium-ion batteries. *Nano. Res.* **2012,** *5*, 395-401.
15. Lu, Z. Y.; Wang, H. T.; Kong, D. S.; Yan, K.; Hsu, P. C.; Zheng, G. Y.; Yao, H. B.; Liang, Z.; Sun, X. M.; Cui, Y., Electrochemical tuning of layered lithium transition metal oxides for improvement of oxygen evolution reaction. *Nature Communications* **2014,** *5*, 7.
16. Dogangun, M.; Hang, M. N.; Machesky, J.; McGeachy, A. C.; Dalchand, N.; Hamers, R. J.; Geiger, F. M., Evidence for considerable metal cation concentrations from lithium intercalation compounds in the nano−bio interface gap. *J. Phys. Chem. C* **2017,** *121*, 27473-27482.
17. Dogangun, M.; Hang, M. N.; Troiano, J. M.; McGeachy, A. C.; Melby, E. S.; Pedersen, J. A.; Hamers, R. J.; Geiger, F. M., Alteration of membrane compositional asymmetry by LiCoO2 nanosheets. *ACS Nano* **2015,** *9*, 8755-8765.
18. Bozich, J.; Hang, M.; Hamers, R.; Klaper, R., Core chemistry influences the toxicity of multicomponent metal oxide nanomaterials, lithium nickel manganese cobalt oxide, and lithium cobalt oxide to *daphnia magna*. *Environmental Toxicology and Chemistry* **2017,** *36*, 2493-2592.
19. Gunsolus, I. L.; Hang, M. N.; Hudson-Smith, N. V.; Buchman, J. T.; Bennett, J. W.; Conroy, D.; Mason, S. E.; Hamers, R. J.; Haynes, C. L., Influence of nickel manganese cobalt oxide nanoparticle composition on toxicity toward Shewanella oneidensis MR-1: Redesigning for reduced biological impact. *Environ. Sci.: Nano* **2017,** *4*, 636-646.
20. Hang, M. N.; Gunsolus, I. L.; Wayland, H.; Melby, E. S.; Mensch, A. C.; Hurley, K. R.; Pedersen, J. A.; Haynes, C. L.; Hamers, R. J., Impact of nanoscale lithium nickel manganese cobalt oxide (nmc) on the bacterium Shewanella oneidensis MR-1. *Chemistry of Materials* **2016,** *28*, 1092-1100.
21. Li, M.; Liu, J.; Xu, Y.; Qian, G., Phosphate adsorption on metal oxides and metal hydroxides: A comparative review. *Environ. Rev.* **2016,** *24*, 319-332.
22. Borggaard, O. K., The influence of iron oxides on phosphate adsorption by soil. *Journal of Soil Science* **1983,** *34*, 333-341.
23. Ler, A.; Stanforth, R., Evidence for surface precipitation of phosphate on goethite. *Environ. Sci. Technol.* **2003,** *37*.
24. Appel, C.; Rhue, D.; Kabengi, N.; Harris, W., Calorimetric investigation of the nature of sulfate and phosphate sorption on amorphous aluminum hydroxide. *Soil Science* **2013,** *178*, 180-188.
25. Kabengi, N. J.; Chrysochoou, M.; Bompoti, N.; Kubicki, J. D., An integrated flow microcalorimetry, infrared spectroscopy and density functional theory approach to the study of chromate complexation on hematite and ferrihdyrite. *Chemical Geology* **2017,** *464*, 23-33.
26. Kabengi, N. J.; Daroub, S. H.; Rhue, R. D., Energetics of arsenate sorption on amorphous aluminum hydroxides studied using flow adsorption calorimetry. *Journal of Colloid and Interface Science* **2006,** *297*, 86-94.
27. Kabengi, N. J.; Rhue, R. D.; Daroub, S. H., Using flow calorimetry to determine the molar heats of cation and anion exchange and the point of zero net charge on amorphous aluminum hydroxides. *Soil Science* **2006,** *171*, 13-20.
28. Namayandeh, A.; Kabengi, N., Calorimetric study of the influence of aluminum substitution in ferrihydrite on sulfate adsorption and reversibility. *Journal of Colloid and Interface Science* **2019,** *540*, 20-29.
29. Rhue, R. D.; Appel, C.; Kabengi, N., Measuring surface chemical properties of soil using flow calorimetry. *Soil Science* **2002,** *167*, 782-790.
30. Sabur, M. A.; Goldberg, S.; Gale, A.; Kabengi, N.; Al-Abadleh, H. A., Temperature-dependent infrared and calorimetric studies on arsenicals adsorption from solution to hematite nanoparticles. *Langmuir* **2015,** *31*, 2749-2860.
31. Kubicki, J. D.; Paul, K. W.; Kabalan, L.; Zhu, Q.; Mrozik, M. K.; Aryanpour, M.; Pierre-Louis, A.-M.; Strongin, D. R., ATR-FTIR and density functional theory study of the structures, energetics, and vibrational spectra of phosphate adsorbed onto goethite. *Langmuir* **2012,** *28*, 14573-14587.
32. Baker, L. A.; Brezonik, P. L.; Edgerton, E. S., Sources and sinks of ions in a soft water, acidic lake in Florida. *Water Resources Research* **1986,** *22*, 715-722.
33. Kenoyer, G. J.; Anderson, M. P. Groundwater's dynamic role in regulating acidity and chemistry in a precipitation-dominated lake *Journal of Hydrology* **1989,** *109*, 287-306.
34. Chen, H.; Grey, C. P., Molten salt synthesis and high rate performance of the ‘‘desert-rose’’ form of LiCoO2**. *Advanced Materials* **2008,** *20*, 2206-2210.
35. Takahashi, Y. K., N.; Dokko, K.; Nishizawa, M.; Akimoto, J.; Uchida, I., Structure and electron density analysis of electrochemically and chemically delithiated LiCoO2 single crystals. *Journal of Solid State Chemistry* **2007,** *180*, 313-321.
36. Noda, I.; Ozaki, Y., *Two-dimensional correlation spectroscopy – applications in vibrational and optical spectroscopy*. John Wiley & Sons, Ltd: 2004.
37. Chen, W.; Qian, C.; Liu, X.-Y.; Yu, H.-Q., Two-dimensional correlation spectroscopic analysis on the interaction between humic acids and TiO2 nanoparticles. *Environ. Sci. Technol.* **2014,** *48*, 1119-11126.
38. Wu, H.; Gonzalez-Pech, N. I.; Grassian, V. H., Displacement reactions between environmentally and biologically relevant ligands on TiO2 nanoparticles: Insights into the aging of nanoparticles in the environment. *Environ. Sci.: Nano* **2019,** *6*, 489-504
39. Powell, C. J.; Jablonski, A. *Nist electron effective-attenuation-length database*, version 1.3; National Institute of Standards and Technology: Gaithersburg, MD, 2011.
40. Tanuma, S.; Powell, C. J.; Penn, D. R., Calculation of electron inelastic mean free paths (imfps) vii. Reliability of the TPP-2M IMFP predictive equation. *Surf. Interface Anal.* **2003,** *35*, 268-275.
41. Wojdyr, M., Fityk: A general-purpose peak fitting program. *J. Appl. Cryst.* **2010,** *43*, 1126-1128.
42. Maiyalagan, T.; Jarvis, K. A.; Therese, S.; Ferreira, P. J.; Manthiram, A., Spinel-type lithium cobalt oxide as a bifunctional

electrocatalyst for the oxygen evolution and oxygen reduction reactions. *Nature Communications* **2014,** *5*, 1-8.
43. Tang, W.; Liu, L. L.; Tian, S.; Li, L.; Yue, Y. B.; Wu, Y. P.; Guan, S. Y.; Zhu, K., Nano-LiCoO2 as cathode material of large capacity and high rate capability for aqueous rechargeable lithium batteries. *Electrochemistry Communications* **2010,** *12*, 1524-1526.
44. Fernandez-Rodriguez, J. M.; Hernan, L.; Morales, J.; Tirado, J. L., Low-temperature hydrothermal transformations of LiCoO2 and HCoO2. *Mat. Res. Bull* **1988,** *23*, 899-904.
45. Huang, X.; Bennett, J. W.; Hang, M. N.; Laudadio, E. D.; Hamers, R. J.; Mason, S. E., Ab initio atomistic thermodynamics study of the (001) surface of LiCoO2 in a water environment and implications for reactivity under ambient conditions. *The Journal of Physical Chemistry C* **2017,** *121*, 5069-5080.
46. Lowry, G. V.; Hill, R. J.; Harper, S.; Rawle, A. F.; Ogilvie Hendersen, C.; Klaessig, F.; Nobbmann, U.; Sayre, P.; Rumble, J., Guidance to improve the scientific value of zetapotential measurements in NanoEHS. *Environ. Sci.: Nano* **2016,** *3*, 953-965.
47. Swan, J. W.; Furst, E. M., A simpler expression for henry's function describing the electrophoretic mobility of spherical colloids. *Journal of Colloid and Interface Science* **2012,** *388*, 92-94.
48. Bhattacharjee, S., DLS and zeta potential – what they are and what they are not? *Journal of Controlled Release* **2016,** *235*, 337-351.
49. Patel, V. R.; Agrawal, Y. K., Nanosuspension: An approach to enhance solubility of drugs. *J. Adv. Pharm. Tech. Res.* **2011,** *2*, 81-87.
50. Gong, W., A real time in situ ATR-FTIR spectroscopic study of linear phosphate adsorption on titania surfaces. *International Journal of Mineral Processing* **2001,** *63*, 147-165.
51. Tejedor-Tejedor, M. I.; Anderson, M. A., Protonation of phosphate on the surface of goethite as studied by CIR-FTIR and electrophoretic mobility. *Langmuir* **1990,** *6*, 602-611.
52. Connor, P. A.; McQuillan, A. J., Phosphate adsorption onto TiO2 from aqueous solutions: An in situ internal reflection infrared spectroscopic study. *Langmuir* **1999,** *15*, 2916-2921.
53. Goldberg, S.; Sposito, G., On the mechanism of specific phosphate adsorption by hydroxylated mineral surfaces: A review. *Commun. In Soil sci. Plant Anal.* **1985,** *16*, 801-821.
54. Nord, A. G., The structure of cobalt(ii) tetrametaphosphate, Co2 P4 O12. *Crystal Structure Communications* **1982,** *11*, 1467-1474.
55. Nord, A. G.; Stefanidis, T., Structure refinements of Co3(PO4)2. A note on the reliability of powder diffraction studies. *Acta Chemica Scandinavica, Series A* **1983,** *37*, 715-721.
56. Krishnamachari, N.; Calvo, C., The crystal structure of cobalt diphosphate. *Acta Cryst.* **1972,** *B28*, 2883-2891.
57. Alcántara, R.; Lavela, P.; Tirado, J. L.; Zhecheva, E.; Stoyanova, R., Recent advances in the study of layered lithium transition metal oxides and their application as intercalation electrodes. *Journal of Solid State Electrochemistry* **1999,** *3*, 121-134.
58. Zhecheva, E.; Stayanova, R., Li1-x-yHyCoO2: Metastable layered phases obtained by acid digestion of LiCoO2(O3). *Journal of Solid State Chemistry* **1994,** *109*, 47-52.

Insert TOC Image Here